ELSEVIER

International Journal of Heat and Fluid Flow 23 (2002) 572–581

International Journal of HEAT AND FLUID FLOW

www.elsevier.com/locate/ijhff

DNS of a turbulent boundary layer with separation

Michael Manhart *, Rainer Friedrich

Fachgebiet Strömungsmechanik, Technische Universität München, 85747 Garching, Germany

Abstract

The present contribution reports on a direct numerical simulation (DNS) of a turbulent boundary layer that undergoes separation due to the presence of a pressure gradient at a moderate Reynolds number. The variation of the free-stream velocity has been chosen according to an experiment of Kalter and Fernholz (The influence of free-stream turbulence on an axisymmetric turbulent boundary layer in, and relaxing from, an adverse pressure gradient. In: 5th European Turbulence Conference, Siena, 1994). Because of limited computational resources, the momentum thickness Reynolds number at the reference position had to be reduced to $Re_\theta = 870$ which is about half as large as that of the experiment. Nevertheless, a comparison of integral parameters as well as first and higher order moments shows fair agreement between DNS and experiment. An inspection of the momentum balance underlines the prominent role of the Reynolds stresses in controlling the structure and geometry of the separation bubble. Its shape and dynamics are governed by large scale vortices reaching from the wall to the shear layer above it.

1. Introduction

The separation bubble embedded in a turbulent flat plate boundary layer as a result of a streamwise adverse pressure gradient is highly unsteady and characterized by low-frequency oscillations. Flow reversal starts intermittently at a position far upstream of the time-averaged separation line at which the fraction of negative wall shear stress reaches about 50%. The separation line doesn't move forward and backward as a straight line but displays a strongly irregular shape. A common feature of separating flows is the breakdown of the logarithmic law-of-the wall which starts approximately at 1% backflow (Simpson et al., 1977; Simpson, 1989). If the thickness of the recirculation bubble is small compared to the upstream boundary layer thickness, then the backflow seems to be mainly governed by large-scale vortices occuring in the shear layer above the recirculating zone. Simpson et al. (1981) could show that in such a case, the recirculation bubble constitutes a highly active turbulent region governed from outside in which traditional model approaches for attached flows fail completely.

The improvement of turbulence models in such flow regimes requires a deep understanding of the dynamics and mechanisms of separation and reattachment. DNS is a valuable tool to improve our corresponding physical insight because it provides accurate three-dimensional and time-dependent information of the flow variables. Up to now, only a limited number of direct numerical simulations (DNSs) of separated turbulent boundary layers are available. The separation of *turbulent* boundary layers is fundamentally different from that of *laminar* boundary layers that undergo transition between separation and reattachment.

The separation of a turbulent boundary layer has first been numerically analyzed by Coleman and Spalart (1993). Recently, Skote et al. (2000) and Skote and Henningson (2001) performed a DNS of a separated turbulent boundary layer. An extensive study has been performed by Na and Moin (1998) at a low Reynolds number ($Re_\theta = 300$, based on inlet free-stream velocity and momentum thickness). In their study, separation/reattachment have been enforced by a strong adverse/favourable pressure gradient in streamwise direction.

The study presented here is the first DNS that aims at predicting an actually performed experiment of a separated turbulent boundary layer (Kalter and Fernholz, 1994). In comparison to Na and Moin's study, it has a significantly higher Reynolds number and the reattachment occurs in a region with vanishing rather than strong favourable pressure gradient. Therefore, Reynolds stresses play a crucial role in the momentum

* Corresponding author.
E-mail address: michael@flm.mw.tu-muenchen.de (M. Manhart).

0142-727X/02/$ - see front matter
PII: S0142-727X(02)00153-4

balance of the presented flow. This study aims at providing data for improving turbulence models and physical insight into the dynamics of separation and reattachment of this flow.

2. Computational details

The following section describes the numerical method used in the simulations. It consists of a finite-volume method formulated on a non-equidistant staggered mesh. A Poisson equation for the pressure correction is obtained by the projection-method according to Chorin (1968). A local grid refinement has been introduced in order to save computational resources while achieving the required resolution near the wall. This local grid refinement was crucial for performing the present DNS on the available hardware. For an efficient use of the hardware, the code has been fully vectorized and parallelised.

2.1. Basic scheme

The flow variables, velocity components and pressure, are defined on a non-equidistant Cartesian mesh in a staggered arrangement. Principally, velocity components are stored in the centres of cell faces, while pressure is stored in the cell centres. The specific discrete formulations are derived by integrating the Navier–Stokes equations for an incompressible fluid over the corresponding control cells surrounding the definition points of the individual variables. We are using the midpoint rule for approximating the fluxes by the variables. The required interpolations and the approximation of the first derivatives are performed by linear interpolation and second order central finite difference formulations, respectively. This altogether ensures second order accuracy of the spatial discretisation (e.g., Ferziger and Perić, 1997).

The discrete solution is advanced in time by a leapfrog time step which is second order accurate with respect to the convection term.

$$u^{n+1} = u^{n-1} + 2\Delta t\left[C(u^n) + D(u^{n-1}) - G(p^{n+1})\right] \tag{1}$$

C, D and G denote herein the discrete convective, diffusive and gradient operators. The pressure at the new time level $p^{n+1} = p^n + \Delta p^{n+1}$ is determined by the solution of the Poisson equation

$$\mathrm{Div}\left[G(\Delta p^{n+1})\right] = \frac{1}{2\Delta t}\mathrm{Div}\,(u^*), \tag{2}$$

where u^* is an intermediate velocity field obtained by solving Eq. (1) by using the pressure p^n at the known time level. A divergence-free field u^{n+1} is obtained after a velocity correction step

$$u^{n+1} = u^* - 2\Delta t G(\Delta p^{n+1}). \tag{3}$$

The combination of central interpolation and a leapfrog time step is energy conserving for the one-dimensional pure convection equation. This is the reason why it is especially suited for LES and DNS. In combination with the diffusion operator, the leapfrog time step is slightly unstable (compare Fletcher, 1988). Therefore, the diffusive term is taken at the time level $n-1$ in Eq. (1). Every 41 time steps, an averaging step is performed in order to prevent $2\Delta t$ oscillations.

The Poisson equation (2) is solved by an iterative procedure accelerated by a multigrid cycle. The smoother is based on the velocity–pressure iteration presented by Hirt et al. (1975) with overrelaxation. This scheme gives the same convergence properties as a conventional Gauss–Seidel iteration with successive overrelaxation (SOR). The advantage of the present algorithm is the easy treatment of boundaries, at which only velocity boundary conditions have to be specified. In order to improve the convergence of the iterative solver, a multigrid procedure has been implemented.

2.2. Local grid refinement

The introduction of a locally refined grid near the wall is one of the key points for an efficient simulation of the separated turbulent boundary layer. The refinement is achieved by dividing one coarse-grid cell into eight fine-grid cells. The coarse and the fine-grids are arranged in an overlapping way, so that the coarse-grid is defined globally (global grid) and the fine-grid is defined only locally (zonal grid). The coarse-grid and the fine-grid solutions are fully coupled. The coupling is achieved by transferring the fine-grid solution in the overlap region to the coarse-grid each time before the algorithm changes from the fine-grid level to the coarse-grid level. We use averaging over four cell faces for the velocities and averaging over eight grid cells for the pressure restriction. While solving the Poisson equation on both levels, we use the pressure correction on the coarse-grid as a new pressure estimate for the fine-grid in the multigrid cycle.

The treatment of the interface between fine- and coarse-grid needs special attention. It appears at two different positions in the algorithm, (i) as pressure boundary condition for the fine-grid and (ii) as velocity boundary condition for the fine-grid. We are using so-called ghost cells in order to manage the boundary conditions for the grid interface. The situation is displayed for a two-dimensional configuration in Fig. 1. Capital letters indicate coarse-grid variables and small letters indicate fine-grid variables. The fine-grid variables on the left hand side of Fig. 1 are called ghost cells. The coarse-grid variables on the right hand side of Fig. 1 are obtained from the fine-grid variables by a restriction.

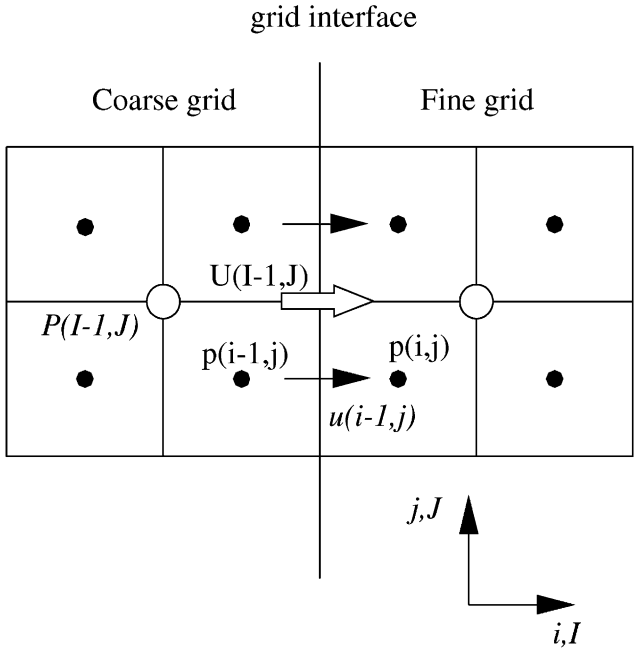

Fig. 1. Configuration of grid interface between local fine- and global coarse-grid.

Due to the staggered arrangement of the variables and the special refinement strategy, both coarse-grid variables as well as fine-grid variables are located on the grid interface.

On the local grid, a Neumann boundary condition is used for the pressure at the fine-grid/coarse-grid interface. It has been found that this treatment is superior to a Dirichlet boundary condition for the fine-grid pressure correction at the grid interface (Manhart, 1998). As a consequence, the fine-grid interface velocities $u(i-1,j)$ and $u(i-1,j+1)$ in Fig. 1 are determined by a suitable conservative prolongation from the coarse-grid interface velocity $U(I-1,J)$. Our tests showed that first order interpolation leads to smaller distortions at the grid interface than second order interpolations due to their inherent damping properties (Manhart, 2002).

The local grid approach has been used successfully for turbulent channel flow (Manhart, 1998), turbulent zero pressure gradient and adverse pressure gradient flow (Manhart, 1999a,b,c). For a more detailed description of the algorithm see (Manhart, 2002).

2.3. Boundary conditions

Since the flow is homogeneous in spanwise direction, periodic boundary conditions are prescribed in this direction. The wall is treated by a no-slip condition. At the outflow, a zero gradient condition is applied for the velocities, which compiles into a Dirichlet condition for the pressure ($p=0$). Due to its non-physical behaviour, this condition produces a distortion of the flow traveling upstream. The region of influence visible in the skin friction coefficient extends over about two inflow boundary layer thicknesses, which is smaller than one outflow boundary layer thickness and corresponds to about 2% of the computational domain (see e.g. Fig. 3).

At the upper boundary of the domain, the vertical velocity is prescribed. It has been obtained from a prior coarse-grid simulation (Manhart and Friedrich, 1999). Due to different sizes of the separation bubbles in the prior and the present simulation, the vertical velocity had to be slightly adjusted in order to obtain the correct streamwise variation of the freestream velocity. In principle, this adjustment could be avoided if the desired streamwise variation of the displacement thickness were known. Lund et al. (1998) (see also Piomelli et al., 2000) proposed a method of determining the vertical velocity through the upper surface by integrating the continuity equation in wall-normal direction. Unfortunately, the streamwise variation of the displacement thickness was not known for the complete flow domain. In the prior simulation, the pressure gradient has been introduced by a Dirichlet condition for the pressure. There, the streamwise variation of the pressure has been derived from the variation of the freestream velocity using Bernoulli's equation. In laminar flows, no difference between the various approaches could be observed. Looking back and comparing the prior simulation with the present one, the use of a Dirichlet condition for the pressure at the upper surface seems to be superior to specifying the vertical velocity component through the upper surface.

Time-dependent inflow profiles are constructed by superposition of a time-mean profile and a fluctuation from a position $10\delta_0$ downstream (where δ_0 is the boundary layer thickness at the inlet plane, see Fig. 2). A detailed description of that method, which is a variant of the method proposed by Schmitt et al. (1986), is given in Manhart and Friedrich (1999). Herein, a comparison with the method proposed by Lund et al. (1998) revealed no significant differences between both approaches.

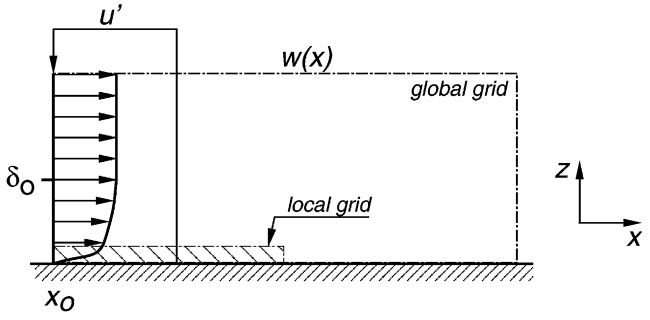

Fig. 2. Geometry of the boundary layer simulations (not to scale).

2.4. Configuration

The simulation presented here is designed according to an experiment performed by Kalter and Fernholz (1994). In this experiment a turbulent boundary layer developing along a circular cylinder ($Re_\theta \approx 1500$) is subjected to a streamwise adverse pressure gradient until separation occurs. In the subsequent nearly zero-pressure gradient region the flow reattaches and slowly relaxes to a canonical boundary layer. The separation bubble is very thin and can be suppressed by a certain level of freestream turbulence. During the separation process the thickness of the boundary layer grows by a factor of about 9.

In the simulation, a rectangular domain has been selected covering the separation bubble. In addition to that, the following simplifications have been introduced. First, a flat plate boundary layer has been simulated instead of a boundary layer along a cylindrical body with spanwise curvature. The effect of this simplification is small because the ratio of boundary layer thickness/diameter is small. Second, the Reynolds number has been lowered in the simulation compared to the experiment, which may lead to some changes in the size of the separation bubble. So, we do not expect a one-to-one quantitative correspondence between simulation and experiment. A third difference between experiment and simulation arises from the inherent presence of a small amount of freestream turbulence in the experiment. Although at a very low level (≈0.5%), this freestream turbulence might have some influence on the evolution of the separation bubble since the latter is very sensitive to the freestream turbulence level (Kalter and Fernholz, 1994).

In terms of boundary layer thickness at the inlet δ_0, the reference position x_r in the simulation is located $10\delta_0$ downstream of the inlet (at $x/\delta_0 = 5.0$). Using the freestream velocity U_0 at the inlet, the Reynolds numbers at this position are $Re_\theta = 870$ and 1560 in the simulation and the experiment, respectively. The Reynolds number based on wall friction velocity is $Re_\tau = 319$ at the reference position. In terms of the displacement thickness δ^*_r at the reference position, the dimensions of the computational box are $L_x = 542\delta^*_r$ in streamwise, $L_y = 128\delta^*_r$ in spanwise and $L_z = 54\delta^*_r$ in vertical direction. In what follows, all quantities are normalized by U_0 and δ_0, respectively ($\delta^*_r/\delta_0 = 0.188$).

We performed a preliminary simulation, denoted here as "coarse DNS" (Manhart and Friedrich, 1999), in which a zonal grid covered the wall region from the inflow to the outflow plane. An analysis of the directional dissipation scale (see Manhart, 2000) in this simulation revealed that the local grid is necessary only in the first half of the computational domain. A second finer DNS was designed in which the zonal grid covers only the first half of the computational domain (Fig. 2).

Table 1
Parameters of the numerical grids

	NX	NY	NZ	Δx^+	Δy^+	Δz^+
Coarse						
Global	640	320	96	52.8	24.8	6.6
Local	1280	640	32	26.4	12.4	3.3
Fine						
Global	1280	448	160	25.5	17.2	3.2
Local	1280	896	32	11.7	7.2	1.6

Inner coordinates are based on the friction velocity at the reference position.

The parameters of both simulations are shown in Table 1. With a wall normal grid spacing at the reference position x_r of $\Delta z^+_{min} = 1.6$, the position of the first grid point is at $z^+ = 0.8$. The simulations were carried out on a Fujitsu VPP/700 vector-parallel computer. By using 16 processors, about 12 G flop/s were achieved. One time step of $\Delta t\, U_0/\delta_0 = 0.005$ took about 28 CPU-s. The present simulation would not have been possible without the use of a local grid refinement on the available hardware, since it saved a factor of more than three in computational resources.

3. Results

3.1. Global flow description

In Fig. 3, the distributions of the free-stream velocity U_∞ and the skin friction coefficient c_f are shown. Unlike in the simulation of Skote et al. (2000) and Skote and

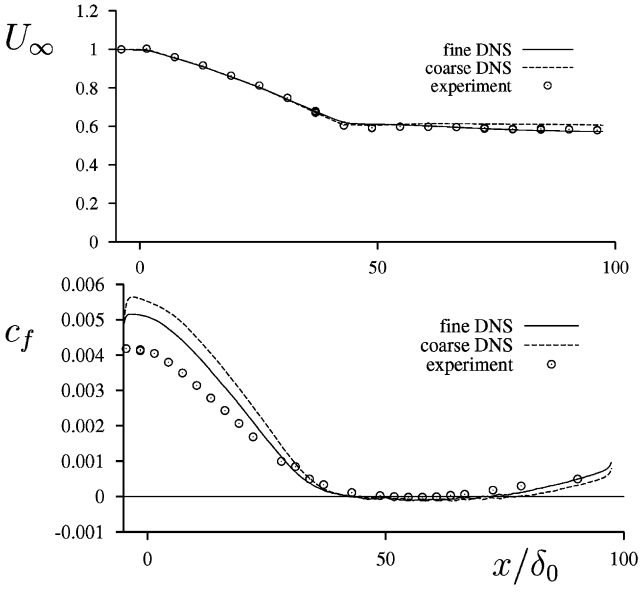

Fig. 3. Distribution of free-stream velocity (top) and skin friction coefficient (bottom) in the separated turbulent boundary layer.

Henningson (2001), there is no power-law variation of the freestream velocity, which gives rise to a continuously changing pressure gradient parameter β. Compared to the simulation of Na and Moin (1998), the deceleration of the freestream velocity is considerably smaller.

Since there is no noticeable variation of the freestream velocity after separation ($x/\delta_0 \approx 40$), the boundary layer is slowly relaxing from the separated regime by diffusive and convective processes only. This leads to a long regime where c_f is nearly zero. In both simulations, the separation bubble as measured by a negative c_f-value is a little bit longer than in the experiment. The length of the recirculation zone doesn't seem to be appreciably influenced by the grid resolution. As seen in an analysis of the spanwise energy spectra in the prior coarse-grid simulation (Manhart and Friedrich, 1999), the grid resolution requirements become increasingly less demanding as one approaches the separation zone.

The improvement of c_f by the use of a finer grid is clearly visible in the upstream regime where the adverse pressure gradient sets in. The difference between fine-grid DNS and experiment can be attributed to the different Reynolds numbers. Coles' empirical correlation (Coles, 1962) gives values of $c_f \approx 0.004$ for $Re_\theta = 1500$ which corresponds to the experiment and $c_f \approx 0.0047$ for $Re_\theta = 870$ which corresponds to our DNS. The coarse-grid simulation produces a c_f-value too high in this region. It is slowly approaching the more realistic value of the fine-grid DNS and, surprisingly, reaches separation at the same streamwise position. The relative unimportance of the grid resolution on the recirculation length leaves one main reason for the larger separation region in the simulation, namely the lower Reynolds number.

The displacement thickness δ^*/δ_0 and the momentum thickness θ/δ_0 are shown in Fig. 4. Both are rather unaffected by grid resolution and in good agreement with the experiment. The displacement thickness reaches a maximum value in the separation region, where it has grown by a factor of about 20 from its initial value. This clearly shows the need for a large computational domain both, in wall-normal and spanwise directions.

The streamlines of the averaged velocity field in Fig. 5 display the geometry of the separation bubble by the intersection points between the wall and the dividing streamline. According to the definition of Simpson (1996), the positions indicated in the Figure are incipient detachment (ID, 1% backflow), intermittent transitory detachment (ITD, 20% backflow) and transitory detachment (TD, 50% backflow). TD is at the same position as $\tau_w = 0.0$ which denotes detachment or separation (at $x/\delta_0 = 44$). The flow reattaches at $x/\delta_0 = 72$. The height of the separation bubble is about δ_0 (strong separation).

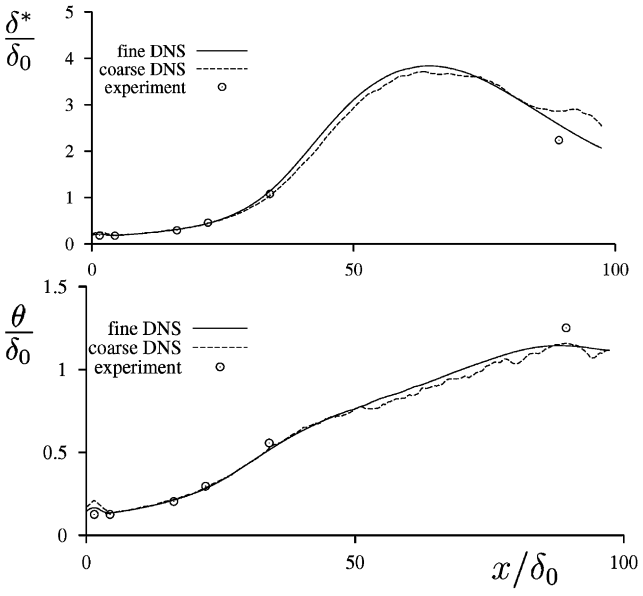

Fig. 4. Displacement (top) and momentum (bottom) thickness in the separated turbulent boundary layer.

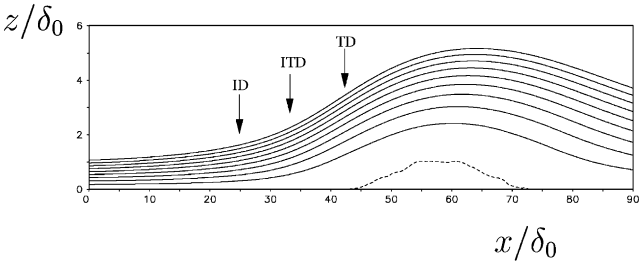

Fig. 5. Streamlines of averaged velocity field with various positions of detachment according to Simpson (1996). The dashed line shows the dividing streamline ($\Psi = 0$).

3.2. First- and higher-order moments

Profiles of streamwise velocity averaged in time and spanwise direction are compared in Fig. 6 with experimental data. Two positions are located in the adverse pressure gradient region ($x/\delta_0 = 22$ and 34) and one after reattachment ($x/\delta_0 = 90.0$). In the separation zone, no experimental profiles are available. Before separation, good accordance between all results has been achieved. After reattachment, the profiles differ due to the different lengths of computed and measured separation bubbles. The profiles are still relaxing towards a canonical zero pressure gradient boundary layer. Fig. 7 shows, how the profiles of the DNS (fine) approach the experimental one at $x/\delta_0 = 90$ with increasing distance from the reattachment point. Unfortunately, the computational resources did not allow for a longer domain to capture more of the downstream development of the relaxing boundary layer. A normalization of the positions with the corresponding bubble length and a com-

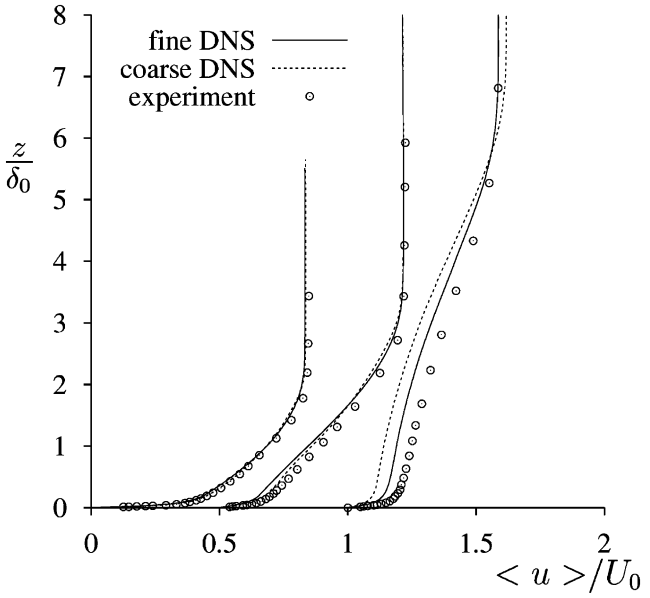

Fig. 6. Averaged streamwise velocity profiles in comparison with the experiment of Kalter and Fernholz (1994); from left to right: $x/\delta_0 = 22$, 34 and 90 (profiles are shifted by $\langle u \rangle / U_0 = 0.5$).

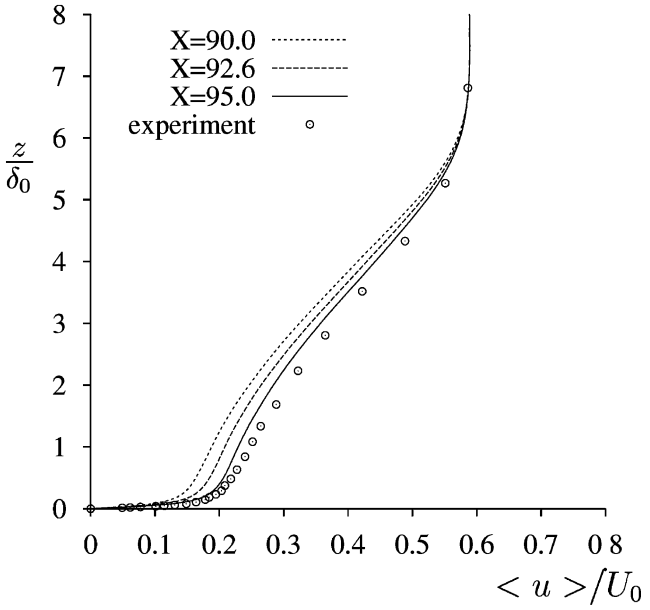

Fig. 7. Averaged streamwise velocity profiles in comparison with the experiment of Kalter and Fernholz (1994) (at $x/\delta_0 = 90.0$); DNS profiles from left to right: $x/\delta_0 = 90.0$, 92.6 and 95.0.

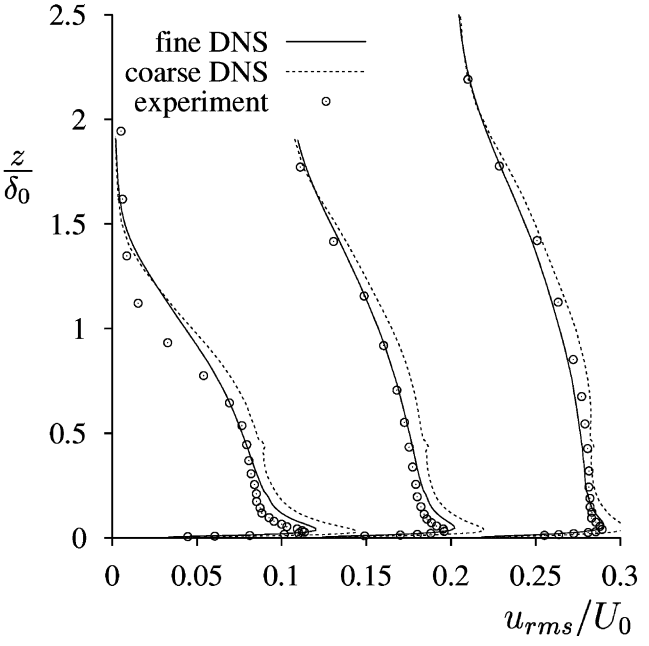

Fig. 8. RMS of the streamwise velocity component in comparison with the experiment of Kalter and Fernholz (1994); from left to right: $x/\delta_0 = 4$, 16 and 22 (profiles are shifted by $u_{\mathrm{rms}}/U_0 = 0.1$).

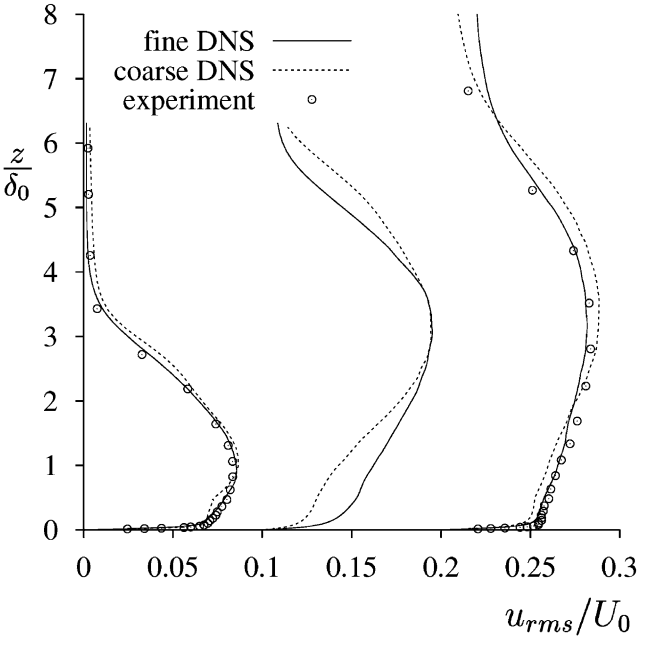

Fig. 9. RMS of the streamwise velocity component in comparison with the experiment of Kalter and Fernholz (1994); from left to right: $x/\delta_0 = 34$, 50 and 90 (profiles are shifted by $u_{\mathrm{rms}}/U_0 = 0.1$).

parison at equal normalized positions would perhaps provide better agreement. With this scaling, however, the measuring position ($x/\delta_0 = 90$) lies outside the computational domain.

The RMS-values of the streamwise velocity fluctuations are shown in Figs. 8 and 9. A significant grid dependence of the profiles can be observed. The coarse-grid produces too high near-wall peaks and a bump at the location of the zonal/global grid interface (at $z/\delta_0 = 0.44$). The fine-grid shows only a small step at the interface which is only visible at $x/\delta_0 = 4$. This step can be explained by the additional small scale energy resolved by the finer local grid. At upstream positions

($x/\delta_0 < 16$), the near-wall peak in the fine DNS is higher than in the experiment. This is not due to a poor grid resolution, but rather a Reynolds number effect. The same Reynolds number dependence of the peak RMS-value can also be observed in results reported by Fernholz and Finley (1996) or in the data of Spalart (1988) (when plotted in outer variables). By the action of the pressure gradient, the peak of the RMS values moves away from the wall in accordance with the growth of the boundary layer thickness.

Further assessment of the simulation data is made by comparing higher order moments of the streamwise velocity component. We took 1656 statistically independent samples for the higher moments which covered a time of $828\delta_0/U_0$. This still seems to be insufficient to reach a fully converged state as can be seen by the inclusion of the moments after 357 samples in the plots. Nevertheless, the accordance between DNS and experiment is satisfying. The large negative peaks in the skewness (Fig. 10) mark the edge of the boundary layer. Throughout the boundary layer, the skewness is small, reaching strong positive peaks at the wall, indicating remarkable non-Gaussianity only close to the wall and at the boundary layer edge. In the flatness profiles (Fig. 11), the boundary layer edge is marked by strong positive peaks. The main part of the boundary layer is near a value of 3, indicating Gaussianity. Again, near the wall, larger values show the loss of Gaussianity, like it is observed in many other studies of wall turbulence.

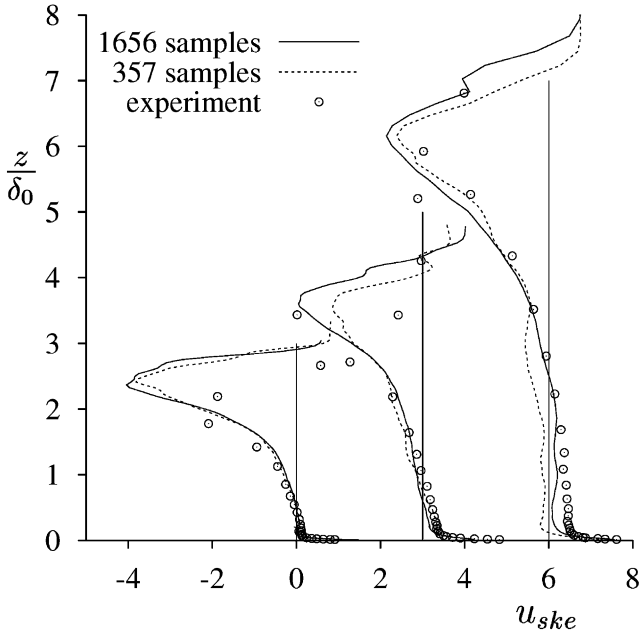

Fig. 10. Skewness of the streamwise velocity component in comparison with the experiment of Kalter and Fernholz (1994); from left to right: $x/\delta_0 = 22$, 34 and 90 (profiles are shifted by $u_{ske}/U_0 = 3.0$).

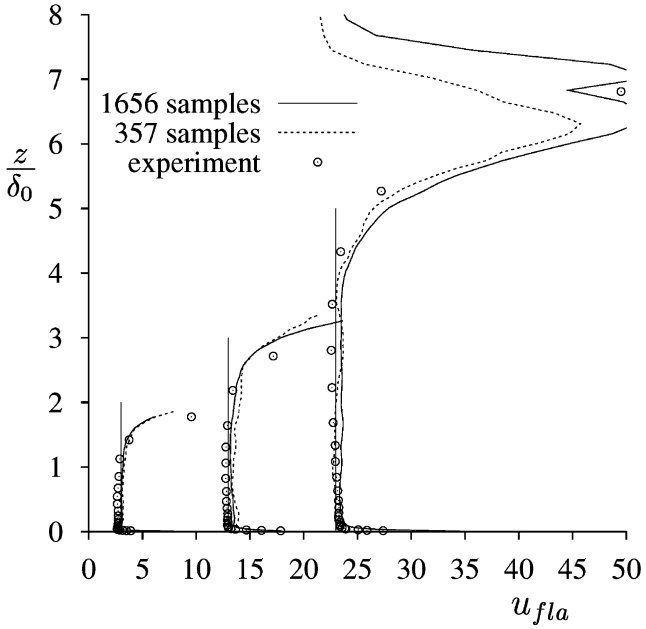

Fig. 11. Flatness of the streamwise velocity component in comparison with the experiment of Kalter and Fernholz (1994); from left to right: $x/\delta_0 = 22$, 34 and 90 (profiles are shifted by $u_{fla}/U_0 = 10.0$).

3.3. Momentum balance

In order to shed some light on the internal structure of the flow during the deceleration, separation and reattachment, we consider the mean streamwise momentum balance

$$0 = \underbrace{-\left(\frac{\partial UU}{\partial x} + \frac{\partial UW}{\partial z}\right)}_{C_1} \underbrace{-\frac{1}{\rho}\frac{\partial P}{\partial x}}_{P_1} \underbrace{+\nu\left(\frac{\partial^2 U}{\partial x^2} + \frac{\partial^2 U}{\partial z^2}\right)}_{D_1} \underbrace{-\frac{\partial \overline{u'u'}}{\partial x} - \frac{\partial \overline{u'w'}}{\partial z}}_{R_1} \tag{4}$$

The individual terms herein are identified as convection (C_1), pressure (P_1), viscous (D_1) and Reynolds (R_1) term. We plot profiles of the individual terms in the Figs. 12–14. The incoming flow corresponds to a zero pressure gradient boundary layer, where close to the wall viscous and Reynolds stresses are in balance. This structure is changed during the deceleration of the boundary layer ($x/\delta_0 = 34.0$, Fig. 12) by the action of the adverse pressure gradient which is in balance with the convective term outside of the boundary layer. Since the pressure term is nearly constant throughout the layer, its decelerating effect is constant. Within the boundary layer, the Reynolds term is positive close to the wall and negative in the outer layer. This term transports momentum to the wall and is the only process to delay separation.

Within the separation bubble ($x/\delta_0 = 50.0$, Fig. 13), the decelerative effect of the pressure gradient is still present, but much weaker. The Reynolds term has be-

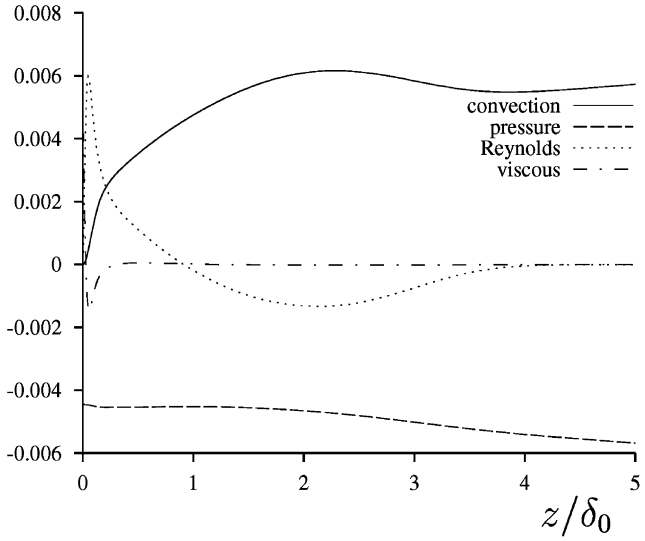

Fig. 12. Mean streamwise momentum balance normalized by U_0^2/δ^* before separation ($x/\delta_0 = 34$).

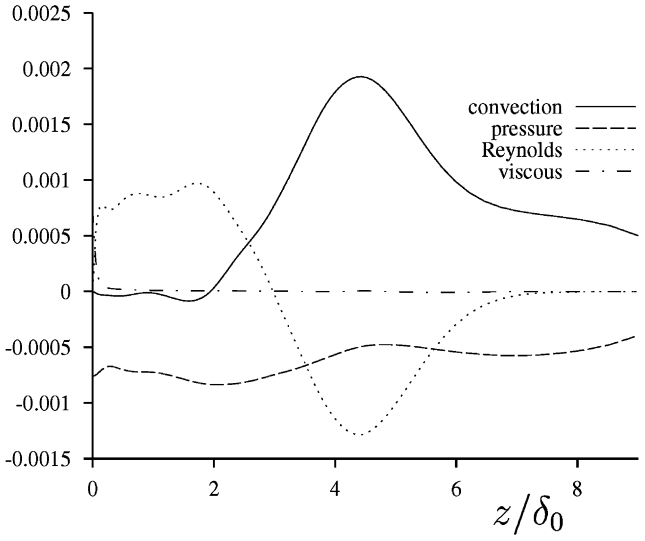

Fig. 13. Mean streamwise momentum balance normalized by U_0^2/δ^* in the separation bubble ($x/\delta_0 = 50$).

come increasingly important for the momentum balance. Within the recirculation zone ($z/\delta_0 \leqslant 2.0$), this term balances the weak adverse pressure gradient and is the only term to transport momentum, since the convection term vanishes. The free shear layer surrounding the recirculation zone is characterized by peak values in the counteracting convection and Reynolds stress terms. A similar flow behaviour can be observed in recirculation zones generated by backsteps (Le et al., 1997).

After reattachment, the boundary layer is slowly relaxing towards its zero pressure gradient state. Within the computational domain ($x/\delta_0 = 90.0$, Fig. 14), the internal momentum balance is however still fundamentally different from that of a zero pressure gradient

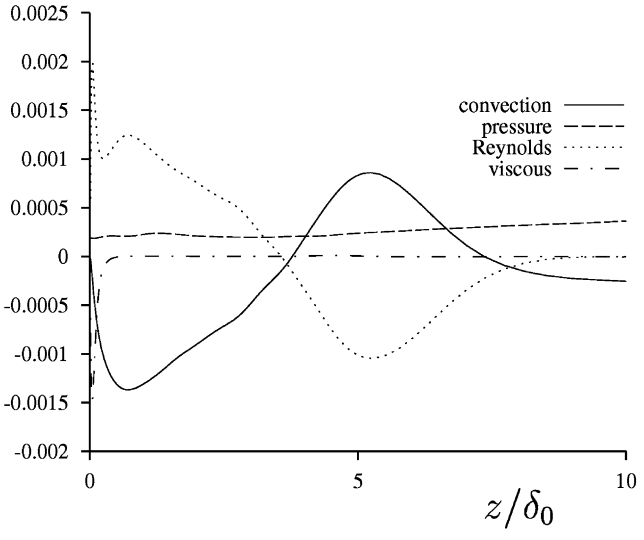

Fig. 14. Mean streamwise momentum balance normalized by U_0^2/δ^* after reattachment ($x/\delta_0 = 90$).

boundary layer. Besides this, there is a weak accelerating pressure gradient. An interesting feature of this relaxing boundary layer is the change in sign of the convective and Reynolds terms. In fact, the two convective terms are counteracting with $-\partial UU/\partial x$ being negative and $-\partial UW/\partial z$ being positive. For $z/\delta_0 > 4.0$ the latter is stronger than the former, which gives the change in sign. This entrains a similar behaviour in the Reynolds stress term, since other terms are small.

3.4. Instantaneous structure of the separation bubble

The separation and reattachment lines are not fixed in space and time. In order to get an impression of the complicated nature of the instantaneous shape of the separation bubble, we show grey-scale plots of the instantaneous streamwise velocity component. In Fig. 15, perspective views of the streamwise velocity component in planes vertical to the coordinate axes are shown. Different velocity magnitudes are coded by different grey scales. The freestream velocity is coded by a mild grey, slow velocities by dark tones. The backflow velocities are indicated by white spots within the dark, nearly black regions. In this view, the strong thickening of the boundary layer during the separation process becomes obvious. This is connected with the growth of large scale structures due to deceleration, which extend throughout the whole layer from the wall to the shear layer above the separation zone. The instantaneous shape of the separation bubble is displayed in Fig. 16 by a top view of the isosurface of $u = 0.0$. The main feature emanating from the pictures is the highly irregular shape of the separation bubble. At the instant shown, the separation line meanders between $x/\delta_0 = 40$ and 50 with a dominant spanwise wavelength of $5\delta^*$ (in terms of local

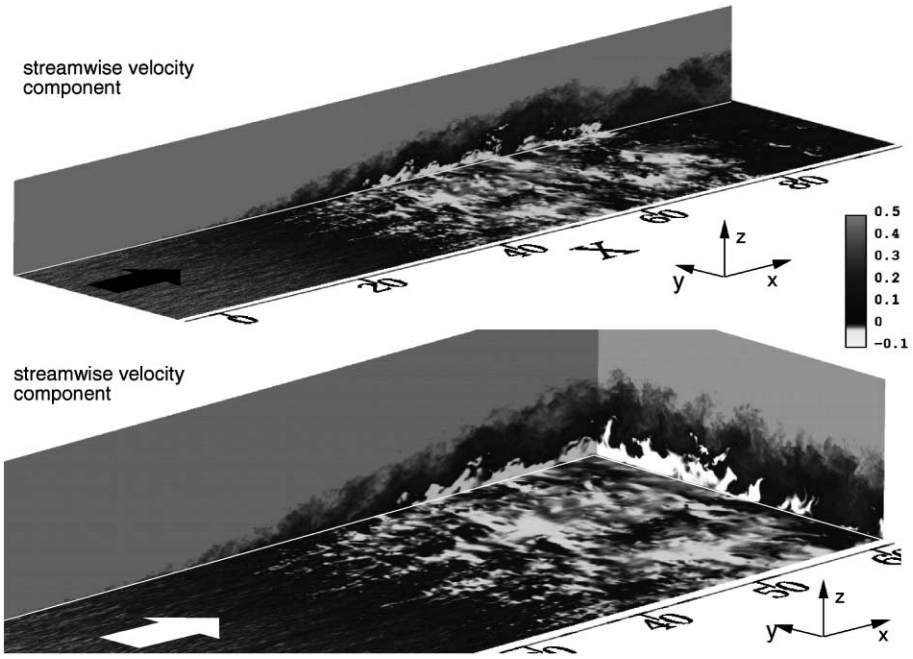

Fig. 15. Instantaneous velocity fields: perspective view of streamwise velocity component. Whole domain (top) and zoom (bottom).

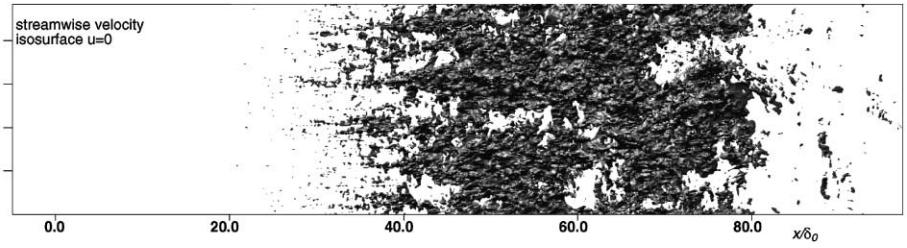

Fig. 16. Instantaneous velocity fields: top view of isosurface $u = 0.0$ of streamwise velocity component.

displacement thickness). The holes in the zero-velocity surface are generated by blobs of forward flow reaching down to the wall. This supports the idea of a strong vertical momentum transport in the free shear layer through which positive streamwise momentum even reaches the wall.

4. Conclusions

We have performed a DNS of a fully turbulent flat plate boundary layer with separation as a result of a streamwise adverse pressure gradient. After reattachment, the boundary layer slowly relaxes to a zero-pressure gradient flow. To our knowledge, this is the first DNS of such a flow which is comparable to a real experiment. The accordance with the experiment is satisfying so that the DNS data can serve as a basis for investigating turbulence models. The DNS gives a slightly longer separation bubble than the experiment which can be attributed to the lower Reynolds number in the DNS. Ongoing investigations using LES will shed more light on the sensitivity of the separation bubble to the Reynolds number.

Profiles of the momentum balance show an essential part of the physics of this particular flow. The separation length is determined mainly by the action of the Reynolds stresses which points towards a sensitivity of the separation bubble to the level of oncoming turbulence for this flow. The separation bubble shows a complicated spatial structure including large-scale variations in spanwise direction and large vortices reaching from the shear layer above the backflow region down to the wall. A more detailed analysis is subject of current work considering the structure and dynamical features of the separation and reattachment process. The investigation of the near-wall behaviour during separation and reattachment in that flow has led to the proposal of a new wall model for large-eddy simulation (Manhart, 2001).

References

Chorin, A.J., 1968. Numerical solution of the Navier–Stokes equations. Math. Computat. 22, 745–762.

Coleman, G., Spalart, P., 1993. Direct numerical simulation of a small separation bubble. In: Speziale, C., Launder, B. (Eds.), Near-Wall Turbulence Flows. Elsevier, Amsterdam, pp. 277–286.

Coles, D., 1962. The turbulent boundary layer in a compressible fluid. In: Report R-403-PR. The Rand Corporation, Santa Monica, CA.

Fernholz, H., Finley, P., 1996. The incompressible zero-pressure-gradient turbulent boundary layer: an assessment of the data. Prog. Aerosp. Sci. 32, 245–311.

Ferziger, J., Perić, M., 1997. Computational Methods for Fluid Dynamics, second ed. Springer, Berlin.

Fletcher, C.A.J., 1988. Computational Techniques for Fluid Dynamics. Springer, Berlin.

Hirt, C., Nichols, B., Romero, N., 1975. Sola—a numerical solution algorithm for transient fluid flows. Los Alamos Sci. Lab, Los Alamos.

Kalter, M., Fernholz, H., 1994. The influence of free-stream turbulence on an axisymmetric turbulent boundary layer in, and relaxing from, an adverse pressure gradient. In: 5th European Turbulence Conference, Siena, 1994.

Le, H., Moin, P., Kim, J., 1997. Direct numerical simulation of turbulent flow over a backward-facing step. J. Fluid Mech. 330, 349–374.

Lund, T., Wu, X., Squires, K., 1998. Generation of turbulent inflow data for spatially developing boundary layer simulations. J. Comp. Phys. 140, 233–258.

Manhart, M., 1998. Zonal direct numerical simulation of turbulent plane channel flow. Computation and visualization of three-dimensional vortical and turbulent flows. In: Friedrich, R., Bontoux, P. (Eds.), Proceedings of the Fifth CNRS/DFG Workshop on Numerical Flow Simulation. vol. 64 of Notes on Numerical Fluid Mechanics. Vieweg Verlag, Braunschweig.

Manhart, M., 1999a. Direct numerical simulation of an adverse pressure gradient turbulent boundary layer on high performance computers. In: Krause, E., Jäger, W. (Eds.), High Performance Computing in Science and Engineering '99. Springer, Berlin, pp. 315–326.

Manhart, M., 1999b. Direct numerical simulation of turbulent boundary layers on high performance computers. In: Krause, E., Jaeger, W. (Eds.), High Performance Computing in Science and Engineering 1998. Springer Verlag, Berlin.

Manhart, M., 1999c. Using zonal grids for direct numerical simulation of turbulent boundary layers with pressure gradients. In: Nitsche, W., Heinemann, H.J., Hilbig, R. (Eds.), vol. 72, Notes on Numerical Fluid Mechanics. Vieweg Verlag, Braunschweig, pp. 299–306.

Manhart, M., 2000. The directional dissipation scale: a criterion for grid resolution in direct numerical simulations. In: Dopazo, C. et al. (Eds.), Advances in Turbulence VIII Eighth European Turbulence Conference. CIMNE, Barcelona, pp. 667–670.

Manhart, M., 2001. Analysing near-wall behaviour in a separating turbulent boundary layer by DNS. In: Geurts, B., Friedrich, R., Metais, O. (Eds.), Direct and Large-Eddy Simulation IV. Kluwer Academic Publishers, Dordrecht.

Manhart, M., 2002. A zonal grid algorithm for DNS of turbulent boundary layers. Comput. Fluids, submitted.

Manhart, M., Friedrich, R., 1999. Towards DNS of separated turbulent boundary layers. In: Voke, P., Sandham, N., Kleiser, L. (Eds.), Direct and Large-Eddy Simulation III. Kluwer Academic Publishers, Dordrecht, pp. 429–440.

Na, Y., Moin, P., 1998. Direct numerical simulation of a separated turbulent boundary layer. J. Fluid Mech. 370, 175–201.

Piomelli, U., Balaras, E., Pascarelli, A., 2000. Turbulent structures in accelerating boundary layers. J. Turbulence 1, 1–16.

Schmitt, L., Richter, K., Friedrich, R., 1986. Large-eddy simulation of turbulent boundary layer and channel flow at high Reynolds number. In: Schumann, U., Friedrich, R. (Eds.), Direct and Large Eddy Simulation of Turbulence. Vieweg, Braunschweig, pp. 161–176.

Simpson, R., 1989. Turbulent boundary-layer separation. Ann. Rev. Fluid Mech. 21, 205–234.

Simpson, R., 1996. Aspects of turbulent boundary-layer separation. Prog. Aerosp. Sci. 32, 457–521.

Simpson, R., Chew, Y., Shivaprasad, B., 1981. The structure of a separating turbulent boundary layer. Part I: mean flow and Reynolds stresses. J. Fluid Mech. 113, 23–51.

Simpson, R., Strickland, J., Barr, P., 1977. Features of a separating turbulent boundary layer in the vicinity of separation. J. Fluid Mech. 79, 553–594.

Skote, M., Henningson, D., Hirose, N., Matsuo, Y., Nakamura, T., 2000. Parallel DNS of a separating turbulent boundary layer. In: Proceedings of the Parallel CFD 2000. NTNU, Trondheim, Norway.

Skote, M., Henningson, D.S., 2001. DNS of a separating turbulent boundary layer. In: Lindborg, E. et al. (Eds.), Turbulence and shear flow phenomena. Second International Symposium. KTH, Stockholm.

Spalart, P., 1988. Direct simulation of a turbulent boundary layer up to $R_\theta = 1410$. J. Fluid Mech. 187, 61–98.